

## Article

# Automatic Grape Cluster Detection Combining YOLO Model and Remote Sensing Imagery

Ana María Codes-Alcaraz <sup>1</sup>, Nicola Furnitto <sup>2</sup>, Giuseppe Sottosanti <sup>2</sup>, Sabina Failla <sup>2</sup>, Herminia Puerto <sup>1</sup>, Carmen Rocamora-Osorio <sup>1</sup>, Pedro Freire-García <sup>3</sup> and Juan Miguel Ramírez-Cuesta <sup>2,\*</sup>

<sup>1</sup> Centro de Investigación e Innovación Agroalimentaria y Agroambiental (CIAGRO-UMH), Miguel Hernández University, 03312 Orihuela, Spain; acodes@umh.es (A.M.C.-A.); hpuerto@umh.es (H.P.); rocamora@umh.es (C.R.-O.)

<sup>2</sup> Department of Agriculture, Food and Environment (Di3A), University of Catania, 95123 Catania, Italy; nicola.furnitto@phd.unicit.it (N.F.); giuseppe.sottosanti@unicit.it (G.S.); sfailla@unicit.it (S.F.)

<sup>3</sup> Centro de Investigaciones sobre Desertificación (CIDE), CSIC-UV-GVA, Carretera CV 315, km 10.7, 46113 Valencia, Spain; pedfefre@gmail.com

\* Correspondence: jm.ramirezcuesta@unicit.it

**Abstract:** Precision agriculture has recently experienced significant advancements through the use of technologies such as unmanned aerial vehicles (UAVs) and satellite imagery, enabling more efficient and precise agricultural management. Yield estimation from these technologies is essential for optimizing resource allocation, improving harvest logistics, and supporting decision-making for sustainable vineyard management. This study aimed to evaluate grape cluster numbers estimated by using YOLOv7x in combination with images obtained by UAVs from a vineyard. Additionally, the capability of several vegetation indices calculated from Sentinel-2 and PlanetScope satellites to estimate grape clusters was evaluated. The results showed that the application of the YOLOv7x model to RGB images acquired from UAVs was able to accurately predict grape cluster numbers ( $R^2$  value and RMSE value of 0.64 and 0.78 clusters vine $^{-1}$ ). On the contrary, vegetation indexes derived from Sentinel-2 and PlanetScope satellites were found not able to predict grape cluster numbers ( $R^2$  lower than 0.23), probably due to the fact that these indexes are more related to vegetation vigor, which is not always related to yield parameters (e.g., cluster number). This study suggests that the combination of high-resolution UAV images, multispectral satellite images, and advanced detection models like YOLOv7x can significantly improve the accuracy of vineyard management, resulting in more efficient and sustainable agriculture.



Academic Editors: Wen Zhuo, Shibo Fang, Yi Xie and Xiaochuang Yao

Received: 6 December 2024

Revised: 8 January 2025

Accepted: 9 January 2025

Published: 11 January 2025

**Citation:** Codes-Alcaraz, A.M.; Furnitto, N.; Sottosanti, G.; Failla, S.; Puerto, H.; Rocamora-Osorio, C.; Freire-García, P.; Ramírez-Cuesta, J.M. Automatic Grape Cluster Detection Combining YOLO Model and Remote Sensing Imagery. *Remote Sens.* **2025**, *17*, 243. <https://doi.org/10.3390/rs17020243>

**Copyright:** © 2025 by the authors. Licensee MDPI, Basel, Switzerland. This article is an open access article distributed under the terms and conditions of the Creative Commons Attribution (CC BY) license (<https://creativecommons.org/licenses/by/4.0/>).

**Keywords:** object detection; sentinel-2; planetscope; unmanned aerial vehicle; yield estimation

## 1. Introduction

In the current context of agriculture, which is in constant evolution, precision agriculture (PA) has emerged thanks to the strategic combination of intelligent sensors and advanced data analysis to guide agricultural decisions [1]. The purpose of PA is to optimize agricultural practices and management, increase resource efficiency, and reduce environmental impact [2]. This is achieved through the precise application of agricultural inputs only where and when they are needed, thus complying with environmental regulations and promoting sustainable agricultural practices. Additionally, PA addresses climate change through mitigation and adaptation strategies and proactively confronts barriers and challenges in its implementation [3]. This change in agriculture is driven by technologies such as remote sensing, geographic information systems (GISs), Global Positioning Systems (GPSs), big data analysis, Internet of Things (IoT), and artificial intelligence (AI) [4–7].

One of the technologies that has gained significant attention in recent years and has grown in the market is the use of UAVs for digital precision agriculture. Advances in control systems, robotics, electronics, and artificial intelligence have led to the development of sophisticated agricultural unmanned aerial vehicles (UAVs). UAVs offer advantages such as versatility, rapid and accurate remote sensing capabilities, and high-quality imaging at affordable prices. Research trends and patents show growing interest in UAVs for agricultural applications [8]. The use of advanced technologies, such as unmanned aerial vehicles (UAV) and computer vision systems, facilitates the collection of detailed data on soil and crop conditions. This data, analyzed by AI algorithms, allows for informed decisions on crop management, thus optimizing the productivity and sustainability of agricultural operations [9].

Various studies have indicated that UAVs stand out as one of the most effective technologies in precision agriculture, currently in widespread use and deployment [10–14]. These devices are extremely versatile and can perform remote sensing tasks quickly and accurately, even under adverse weather conditions, offering spatial and temporal resolutions that most satellite systems cannot achieve [15]. This high spatial resolution allows the identification of fine details and features that are often imperceptible in satellite images [16]. However, the performance and applicability of these systems depend on multiple factors, such as the weight of the aircraft, payload capacity, size, battery characteristics, flight autonomy under various conditions, acquisition cost, environmental conditions, and specific configurations. From an economic perspective, implementing UAVs in agriculture requires investments in purchasing the platform, additional equipment (such as laser scanners and multispectral or hyperspectral thermal cameras), and hiring a trained pilot both to handle the flight and to process the collected data [8].

The use of artificial intelligence in the viticulture sector is still in its early stages of development. Many processes in viticulture can be significantly improved by the use of artificial intelligence. However, its application has the potential to considerably optimize many processes within viticulture. In recent years, the wine industry has faced serious challenges due to the shortage of qualified labor and rising labor costs, which have affected productivity, wine quality, and timely grape harvesting [17]. Additionally, manual agricultural tasks are time-consuming and subject to the subjective decisions of workers. These problems have incentivized the development of new technologies, such as advanced sensors, including those from UAVs, along with artificial intelligence.

A critical aspect of vineyard management is estimating grape cluster numbers and yield, which is essential for the efficient planning of resources and labor. Traditionally, this task is labor-intensive and time-consuming, involving trained personnel to conduct visual counting on the plot. This has led to the exploration of remote sensing technologies, like the use of UAVs and satellites, offering faster and automated alternatives to manual counting. However, there is still no consensus on whether these technologies are fully capable of providing accurate grape cluster counts. UAVs offer a higher spatial resolution, making them suitable for identifying fine details such as grape clusters, whereas satellite images, with their lower spatial resolution but broader coverage, may contribute useful data on vegetation health and productivity trends over larger areas.

In recent years, the proliferation of modern sensors and the application of new technologies in precision viticulture have resulted in a significant increase in data generation per hectare. This has provided viticulturists with a wealth of information [18]. Data acquisition techniques commonly seen in viticulture can be classified into three groups: satellite imagery, data acquired using aerial platforms (most frequently UAVs), and data collected from terrestrial platforms. Given that vineyards typically cover relatively small areas, the latter two categories play a more important role in evaluating various parameters in

precision viticulture [19]. However, it is worth noting that satellite imagery still has its utility in this field [20].

To compare these data sources for vineyard management applications, it is essential to consider key variables such as ground sampling distance (or spatial resolution), acquired bands, and cost. Free multispectral satellite imagery, such as that provided by the European Union's Copernicus Program (through the Sentinel-2A and 2B satellites), starts at 10 m pixel<sup>-1</sup> and has more bands than typical UAV imagery. Cost is a relevant variable not only for a cost-benefit analysis in the context of user adoption but is also closely related to temporal resolution. The cost of each UAV image limits the number of images throughout the season, while free satellite data is available every five days. Generally speaking, and considering the cost, UAV images have an advantage in spatial resolution, while free Copernicus satellite images have an advantage in temporal resolution.

On the other hand, one of the most frequently raised issues today is the estimation of production on a farm, which is important for the proper management of a farm but involves laborious work that requires time and labor with specific experience or training [21]. Many studies have focused on production estimation by detecting fruits on the trees, including apples, cherries, grapes, avocados, mangoes, and passion fruits, among others [22–26]. Although fruit detection based on deep learning has been successful, inaccurate detection and localization can still occur due to the complexity of agricultural environments, lighting fluctuations, and unpredictability, such as wind or mechanical vibrations during the actual harvesting process [27,28].

In previous studies, grape cluster detection has commonly relied on ground-based imagery [26,29], while UAV imagery combined with NDVI has been used to differentiate live from dry vines [30]. Other authors have used vegetation indices to predict yield, though without direct fruit detection [31]. They revealed that vegetation indices like NDVI face challenges in yield prediction, with performance varying across growth stages and showing inconsistent R<sup>2</sup> values due to factors like climate and reference data. Alternatives like EVI and SAVI also produced contradictory results, further affected by cloud cover, atmospheric conditions, and calibration issues [24,32–36]. This highlights the need to perform grape cluster detection using UAV imagery and to investigate whether there is a relationship between these estimates and vegetation indices, providing a novel perspective for yield estimation.

Single-stage object detection algorithms typically use a neural network to directly predict the positions and categories of all possible bounding boxes in each image [29]. This approach includes the You Only Look Once (YOLO) series [37], which benefits from speed and real-time performance. Various studies have compared different versions of YOLO, such as [38], who compared YOLOv2, YOLOv3, and Mask R-CNN networks in grape detection research, or [39], who employed YOLOv3 for tomato detection using circular rather than traditional rectangular bounding boxes. Moreover, based on YOLOv5, ref. [40] performed lychee detection and calculated pixel coordinates of harvesting points. Currently, the latest version of YOLO is v7, which has been applied for detecting grape maturity in a white grape variety and outperforms other architectures both in precision and accuracy.

For all these reasons, the objectives of this research work were (i) to evaluate the number of grape clusters protected with paper bags estimated by using YOLOv7x in combination with images obtained by UAV from a vineyard and (ii) to assess the potentiality of different vegetation indexes obtained from Sentinel-2 and PlanetScope satellite images to estimate grape cluster number. Novelties of the present study include the use of artificial intelligence and oblique images, which could enhance the grape cluster detection process.

## 2. Materials and Methods

### 2.1. Study Site

The study plot (1.03 ha) is a vineyard (cv. Aledo) located in the municipality of Agost (Alicante, Spain;  $38^{\circ}25'5.46''N$ ;  $0^{\circ}38'22.56''W$ ) (Figure 1). The planting frame is  $1.55\text{ m} \times 2.50\text{ m}$  with a total of 2742 plants, a registered production in 2022 of 12,000 kg, and an average cluster weight of 598 g (average data obtained by the cooperative after weighing 15 clusters). The Bagged Table Grape of Vinalopó used in this study is a unique fruit in the world due to its distinctive ripening process. Unlike other table grapes, the Vinalopó grape grows protected under a paper bag for at least 60 days, preserving each grape in the cluster until it reaches the consumer. Thanks to this particular cultivation method, the Vinalopó table grape possesses exceptional physical and gastronomic characteristics, making it the only bagged grape awarded a Protected Designation of Origin. Additionally, the bag shields the grapes from weather conditions, allowing them to develop much thinner skin, as they do not need to defend against the effects of rain, sun, or wind. This same protection also filters sun exposure, resulting in uniform color across the grapes in each cluster [41].



**Figure 1.** Study site location at Alicante, Spain ( $38^{\circ}25'5.46''N$ ;  $0^{\circ}38'22.56''W$ ); an example of RGB image acquired with the UAV at a height ( $h$ ) of 17 m and a sensor tilt ( $\theta$ ) of  $45^{\circ}$  (green rectangle).

The meteorological conditions registered in the nearest weather station managed by the Sistema de Información Agroclimática para el Regadío (SIAR; <http://riegos.ivia.es/red-siar>, last accessed 5 December 2024), located 1 km far from the experimental plot (Agost weather station, Alicante, Spain;  $38^{\circ}23'12''N$ ;  $0^{\circ}45'28''W$ ) were typical Mediterranean with an average air temperature, relative humidity, wind speed, solar radiation and precipitation of  $17.86\text{ }^{\circ}\text{C}$ ,  $63.81\%$ ,  $1.28\text{ m s}^{-1}$ ,  $16.02\text{ MJ m}^{-2}\text{ day}^{-1}$ , and 338 mm, respectively.

The irrigation system used in this plot was drip irrigation, which is known for its high-frequency water application. This system delivers water directly to the root zone, optimizing its use and minimizing evaporation and deep percolation losses. The seasonal water dose applied was 974 m<sup>3</sup>. The irrigation quantity was managed by the farmer in order to ensure no water stress was observed in the crop.

In addition, it is essential to consider the specific needs of the crop, as well as the efficiency of the soil, which is influenced by its composition. This composition affects the retention and use of water by the plants. Lastly, a water balance is used to compare the water supplied by rainfall with the amount needed by the crop, highlighting the importance of irrigation during months of water deficit.

The soil in the study area was of a limestone nature. Its lithological origin comes from terrace gravel deposits derived from continental sediments, marine sediments, molasses, limestone, and marl with sandstones and limestones. All the soils in the valley have a high calcium carbonate content and low organic matter [42].

## 2.2. UAV Flight Campaign

The aerial images were taken at 10:00 AM (local time) on 27 October 2022, using a UAV Autel EVO 2 pro (UUC Technology Co., Ltd., Hong Kong) equipped with a visible RGB camera with a 1" CMOS sensor (Sony Group Corporation, Tokyo, Japan), adjustable F2.8-F11 aperture capable of 20 megapixels resolution and video recording in 4 K/30 FPS. The UAV flight was conducted following a path parallel to the crop lines. The flight height ( $h$ ) was 17 m, and the sensor tilt ( $\theta$ ) was 45°. To prevent overcounting of grape clusters, the images were captured with a 10% overlapping. The onboard camera obtained these images with a resolution of 3840 × 2160 pixels, resulting in a pixel size of about 1.1 cm. The total flight time was 6.5 min.

## 2.3. YOLO Model

### 2.3.1. Training Pre-Processing

To generate the dataset, the RGB images acquired from the UAV with the flight configuration shown in Figure 1 were used. These images were labeled using the Makesense application (<https://www.makesense.ai/index.html>, accessed on 25 November 2024), a free online photo-tagging tool. As output, grape clusters were annotated with rectangles (Figure 2). A total of 60 images were labeled; these aerial images used for the test were obtained from several flights carried out on different farms with the same flight configuration, where each of the images had 400 labels, out of which 90% were used for training the model and 10% for validation [43,44]. These images were annotated in YOLO format. These images were then resized to 640 × 640 pixels since YOLOv7x is a pre-trained algorithm with an image size of 640 pixels.

The RGB images were subsequently processed using the object detection algorithm known as YOLO. This algorithm is a state-of-the-art single-stage object detection model that approaches detection as a regression problem [37]. This model can detect multiple objects in a single image by dividing the image into a grid. Initially, each grid cell predicts the probability of a class. Then, the model determines bounding box coordinates and calculates confidence scores for each. As a single-stage detector, YOLO models achieve high computational speed [37]. YOLOv7 [45] is an advanced iteration of the widely used YOLO object detection algorithm, known for its single-pass architecture, which enhances efficiency over other object detection methods.

What sets YOLOv7 apart from earlier versions is its superior detection accuracy, which has been achieved through various innovations. These include optimized layer efficiency, effective model scaling techniques, re-parameterization strategies, and the addition of an

auxiliary head with a coarse-to-fine supervision method. Together, these enhancements result in significant performance, efficiency, and adaptability improvements, making YOLOv7 a more effective solution for many practical applications [45]. Within YOLOv7, there are new versions, such as YOLOv7x, which have been shown in various studies to achieve the best results [45]. Specifically, ref. [46] compared two UAV flight configurations, one at 10 m height with a 35° sensor tilt angle and another at 17 m height with a 45° sensor tilt angle, to assess which one provided better detection accuracy. This study concluded that, at 17 m, YOLOv7x performed better than the other evaluated versions (YOLOv7-E6 and YOLOv8), demonstrating greater stability and lower RMSE under this condition. Specifically, the three YOLO versions showed similar mean Average Precisions (mAP) (0.81–0.85), with YOLOv7x presenting the lowest RMSE values (0.78 clusters vine<sup>-1</sup> for YOLOv7x versus 1.39–2.36 clusters vine<sup>-1</sup> for YOLOv7-E6 and YOLOv8). The better performance of YOLOv7x was also observed by [46] when evaluating the total yield estimated from the different YOLO versions. The yield estimates from the YOLOv7x version did not differ from the measured yield, whereas a significant yield underestimation was obtained for the YOLOv7-E6 and YOLOv8 versions at a configuration of 17 m height and 45° sensor tilt angle. Given that the images used in the present study were captured at 17 m, YOLOv7x was chosen as the detection model, as it provided more reliable and consistent results with this flight configuration. The entire process of training the algorithm was carried out on Google Colaboratory, a free platform provided by Google. Google Colaboratory allows users to write and run Python v3.10 code directly from their browser, utilizing resources like Graphics Processing Units and Tensor Processing Units at no additional cost. This makes it an ideal tool for developing and testing machine learning models without the need for personal infrastructure. The training process can be observed in Figure 3.

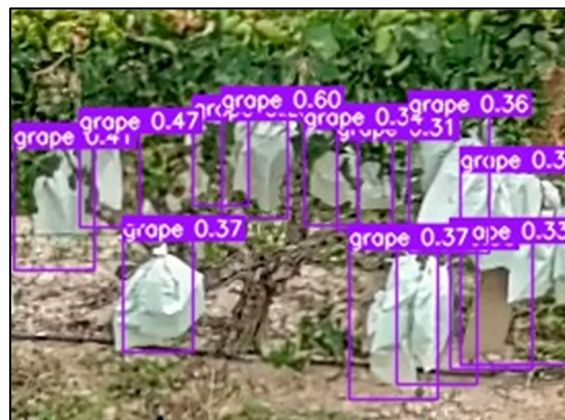


**Figure 2.** Example of cluster detection using YOLOv7x with RGB images acquired from UAV. Numbers in the bounding boxes represent the model's confidence in detecting the objects, expressed as a value between 0 and 1.

### 2.3.2. Performance Metrics

To verify the effectiveness of YOLOv7x model, the accuracy ( $P$ ), recall ( $R$ ), Average Precision ( $AP$ ), detection speed, and F1 score were used in this study.

Specifically,  $P$  is the ratio of true positive samples among all positive samples predicted by the model (Equation (1)). The proportion of true positive samples predicted by the model to all true positive samples is considered by the term  $R$  (Equation (2)). There is usually an inverse correlation between  $P$  and  $R$ . To balance the effects of  $P$  and  $R$  and evaluate a model more holistically,  $AP$  was calculated through the area under the PR curve (Equation (3)), where a higher value means a better model performance. The  $F1_{score}$  (Equation (4)) is the

harmonic mean of  $P$  and  $R$ , providing a balanced assessment of a model's performance while considering both false positives and false negatives (Equation (4)).

$$P = \frac{TP}{TP + FP} 100(\%) \quad (1)$$

$$R = \frac{TP}{TP + FN} 100(\%) \quad (2)$$

$$AP = \int_0^1 P(R) dR \quad (3)$$

$$F1_{score} = \frac{2 \times P \times R}{P + R} \quad (4)$$

where  $TP$ ,  $FP$ , and  $FN$  are the numbers of true positive cases, false positive cases, and false negative cases, respectively [25]. One of the most commonly used metrics for evaluating training is the mAP, which measures the average precision of the model considering different confidence thresholds, with the IoU (Intersection over Union) threshold set at 0.5 in this case. This value, which varies from 0 to 1, reflects the overall performance of the model in correctly identifying grape clusters in most of the analyzed images [45]. In addition, a dataset of 25 images of individual vines was selected to validate the number of grape clusters estimated using the YOLOv7x model. The validation procedure consisted of comparing the estimated value with the grape cluster number obtained in the field by visual counting. The images were carefully selected throughout the entire plot to capture the existing variability in the growing conditions. This strategic selection of images allows for a more representative analysis of the model's effectiveness.

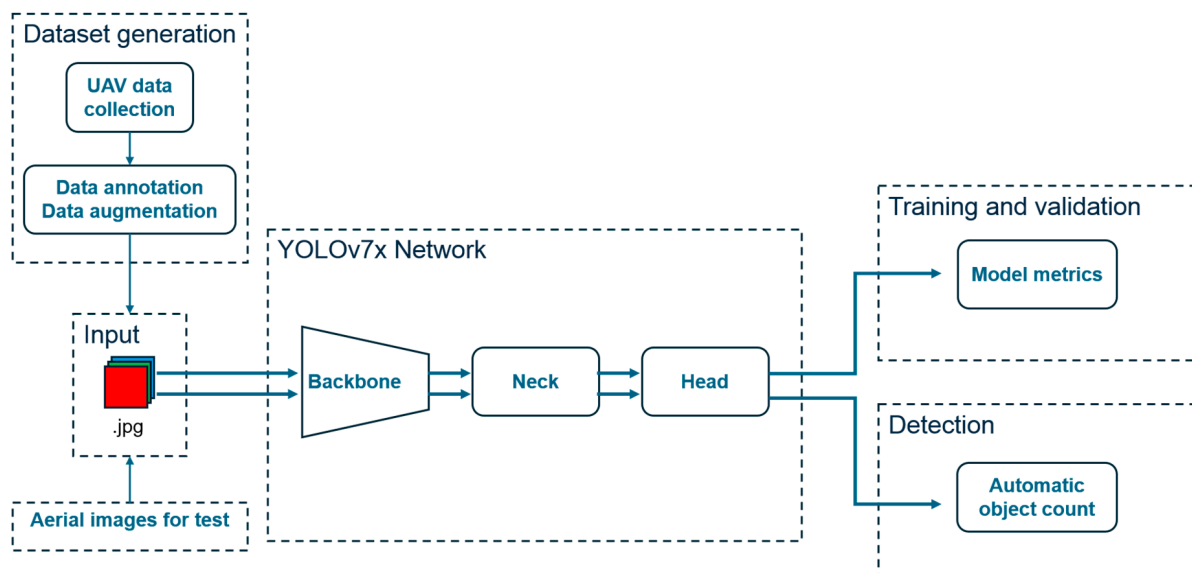


**Figure 3.** Conceptual framework of the object detection methodology.

#### 2.4. Remote Sensing Data

This subsection describes the satellite products utilized for deriving the vegetation indexes and the methodology followed for performing the comparison between such indexes and the grape clusters number derived from the YOLOv7x model.

##### 2.4.1. Sentinel-2 Imagery

Satellites Sentinel-2A and B were used, which have a multispectral instrument on board able to capture imagery across 13 spectral bands with a combined constellation

revisit of five days and a wavelength-dependent spatial resolution from 10 to 60 m [47]. In this study, we used the bands with a spatial resolution of 10 m, which are Band 2—Blue with a Central Wavelength of 490 nm, Band 3—Green 560 nm, Band 4—Red 665 nm, and Band 8—NIR 842 nm [48]. During the study period, 36 cloud-free images were downloaded from the Copernicus Open Access Hub website (<https://scihub.copernicus.eu/>; accessed on 10 July 2024) between February and November 2022. Specifically, Level-2A (L2A) products were considered since they provide images of the bottom of atmosphere reflectance covering the visible and NIR spectral range.

#### 2.4.2. PlanetScope Imagery

PlanetScope SuperDove, a new generation of DOVE CubeSat, was used in this study. The PlanetScope SuperDove instrument, able to image the entire land surface of the Earth every day, has eight spectral bands covering the red edge (705 nm), red (665 nm), green (565 nm), green I (531 nm), yellow (610 nm), blue (490 nm), coastal blue (442 nm), and NIR (865 nm) spectral regions and a pixel size of 3 m [49]. For the period February to November 2022, 100 images of PlanetScope were downloaded from the Planet Explorer website (<https://www.planet.com/explorer/>, accessed on 10 July 2024). Specifically, the PlanetScope Ortho Analytic 8B SR product (level-3B) was used, which offers an orthorectified, scaled Surface Reflectance 8-band image product suitable for analytic applications [50].

#### 2.4.3. Data Processing

ArcGIS 8.3, a geographic information system (GIS) software developed by the Environmental Systems Research Institute (ESRI), was utilized in this study. This software provides a framework for developing customized applications based on existing components [51]. It was employed to extract the Sentinel-2 and PlanetScope bands for each pixel. Initially, the Fishnet tool in ArcGIS was used to map all the vines within the plot, taking into account the planting layout. Subsequently, only the pixels that were fully covered by vines, with no empty spaces, were selected, excluding those on the edge of the plot. This pixel identification was later used to determine the number of grape clusters in each pixel and to associate this information with the Sentinel-2 and PlanetScope bands, enabling a correlation between the two datasets.

Additionally, a point shapefile with the location of each vine was generated, where the number of clusters per vine estimated by the YOLOv7x model was included. To establish the relationship between the estimated cluster number and the different vegetation indexes calculated from the Sentinel-2 and PlanetScope images, the average of the entire study area was considered. The comparative analysis was conducted both for individual dates and for the cumulative value over time.

Based on previous research on yield estimation [52–55], 11 widely used vegetation indices were calculated (Table 1), including the Normalized Difference Vegetation Index (NDVI) [56]; Green Normalized Difference Vegetation Index (GNDVI) [57]; Soil-Adjusted Vegetation Index (SAVI) [58]; Modified Soil-Adjusted Vegetation Index (MSAVI) [59]; Modified Triangular Vegetation Index (MTVI) [60]; Enhanced Vegetation Index (EVI) [61]; Optimized Soil Adjusted Vegetation Index (OSAVI) [62]; Simple Ratio (SR) [63]; and Normalized Difference Water Index (NDWI) [64].

All the UAV images of the plot analyzed by the algorithm were cropped by vines in order to later locate them in the corresponding pixels. This was performed to later correlate them with the vegetation indices obtained from Sentinel-2 and PlanetScope. Figure 2 shows an example of detection from the training. The bounding boxes, generated using the YOLOv7x model with a confidence threshold of 0.25, are overlaid on the image to show the detected objects.

**Table 1.** Vegetation indexes were calculated in the present study. GREEN, RED, and NIR are the spectral bands of Sentinel-2 and PlanetScope satellites corresponding to the green, red, and near-infrared spectral regions (wavelengths of 560, 665, and 842 nm, respectively, for Sentinel 2, and 565, 665, and 865 nm, respectively, for PlanetScope).

Vegetation Indices	Equation	Reference
Normalized Difference Vegetation Index (NDVI)	$\frac{(NIR - RED)}{(NIR + RED)}$	[56]
Soil Adjusted Vegetation Index (SAVI)	$\frac{(1 + 0.5)(NIR - RED)}{NIR + RED + 0.5}$	[58]
Enhanced Vegetation Index (EVI)	$\frac{2.5(NIR - RED)}{(NIR + 6RED - 7.5BLUE + 1)}$	[61]
Green Normalized Difference Vegetation Index (GNDVI)	$\frac{NIR - GREEN}{NIR + GREEN}$	[57]
Modified soil adjusted vegetation index (MSAVI)	$0.5 \left( 2(NIR + 1) - \sqrt{(2NIR + 1)^2 - 8(NIR - RED)} \right)$	[59]
Modified triangular vegetation index (MTVI)	$\frac{1.5[1.2(NIR - GREEN) - 2.5(RED - GREEN)]}{\sqrt{(2NIR + 1)^2 - (6NIR - 5\sqrt{RED})} - 0.5}$	[60]
Normalized Difference Water Index (NDWI)	$\frac{GREEN - NIR}{GREEN + NIR}$	[64]
Optimized Soil-Adjusted Vegetation Index (OSAVI)	$\frac{(NIR - RED)}{NIR + RED + 0.16}$	[62]
Simple Ratio Index (SR)	$\frac{NIR}{RED}$	[63]

To evaluate the performance of the YOLOv7x model in detecting grape clusters, the most common object detection metrics were used: mAP, Precision, Recall, and F1 Score. During the training of the algorithm, each vine within the plot was identified and segmented, and the resulting images were used as input for the algorithm analysis. The algorithm detected and counted the grape clusters of each vine. Then, using a point grid created in ArcGIS, the cluster data for each vine was integrated, generating a map that showed the distribution of vines within the plot, along with the associated cluster number. This method allowed for a precise estimation of the number of vines and grape clusters in each pixel of the image. To calculate the vegetation indices, the spectral band reflectance values from Sentinel-2 and PlanetScope were extracted at the selected pixels in ArcGIS, and the data were transferred to an Excel spreadsheet, where the indices were calculated using the equations shown in Table 1.

### 3. Results

#### 3.1. Model Training and Cluster Detection and Validation

As shown in Figure 4, after experimenting with combinations of batch size and epochs, it was determined that 250 epochs (i.e., number of times the learning algorithm will work on the entire training data set) with a batch size (i.e., number of times an image is divided when being analyzed) of 12 were appropriate for training the YOLOv7x model. In this case, mAP\_0.5 reaches a value of 0.63 at epoch 249. Starting from epoch 249, it can be observed that the graph forms a straight line, indicating that the training will no longer improve.

The precision achieved was 61%, meaning that 61% of the objects detected by the model were indeed grape clusters (true positives). The recall reached 79%, indicating that the model successfully detected 79% of the grape clusters present in the images. Finally, the F1 Score obtained was 66%, which represents the harmonic mean between precision and recall.

The estimated number of clusters per vine varied between 5 and 10, being slightly higher than the measured in the field (4–9 clusters vine<sup>-1</sup>). More specifically, the correlation between estimated and observed values was statistically significant (Figure 5), with an R<sup>2</sup> value and RMSE value of 0.64 and 0.78 clusters vine<sup>-1</sup>, respectively, and had a slope term equal to 0.77 with an intercept value of 1.26 (Table 2).

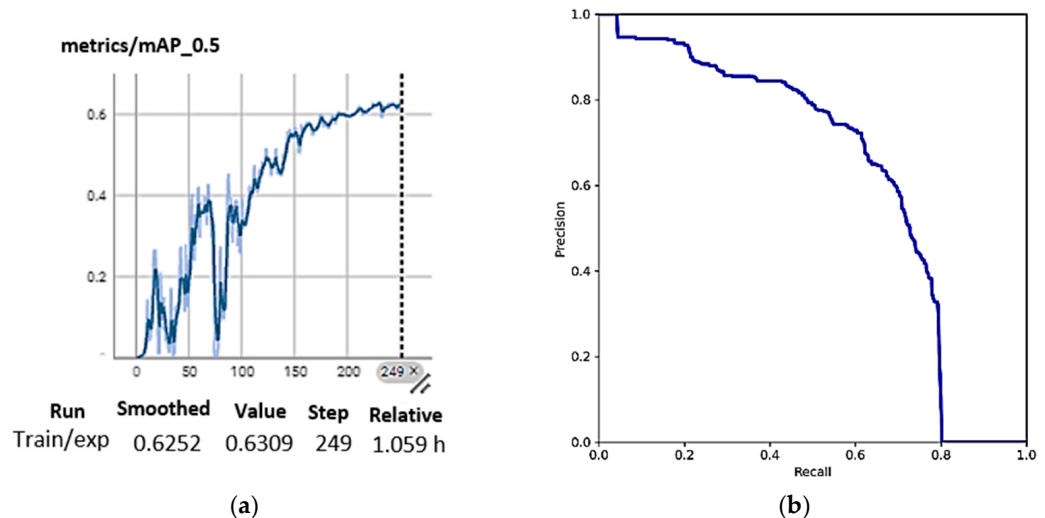


**Figure 4.** (a) Mean Average Precision at an IoU threshold of 0.5, reflecting the model’s detection accuracy, and (b) Precision-Recall Graph indicating the model’s effectiveness in detecting objects.

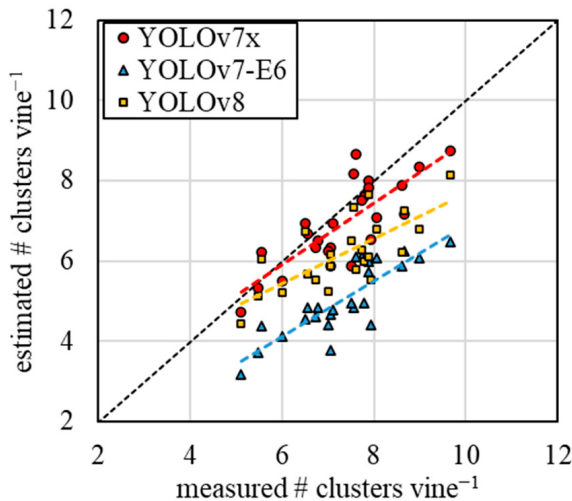


**Figure 5.** Comparison between the number of grape clusters per vine estimated using the YOLOv7x model and the actual measurements observed from the UAV images. The red dashed line represents the trend line regression, while the black dashed line indicates the 1:1 relationship. For comparison purposes, the trend lines obtained by using YOLOv7-E6 (blue dashed line) and YOLOv8 versions (yellow dashed line) have been included (adapted from [46]).

**Table 2.** Correlation equations, coefficient of determination ( $R^2$ ), and Root Mean Square Error (RMSE) for the different YOLO versions (adapted from [46]).

YOLO Version	Equation	$R^2$	RMSE (Cluster Vine $^{-1}$ )
YOLOv7x	$y = 0.77x + 1.26$	0.64	0.78
YOLOv7-E6	$y = 0.69x - 0.04$	0.71	2.36
YOLOv8	$y = 0.56x + 2.10$	0.53	1.39

### 3.2. Comparison of Reflectance in the VIS-NIR Spectral Range Obtained from PlanetScope and Sentinel-2 Satellites

From the comparison between the reflectance values of the Blue, Green, Red, and NIR bands obtained from Sentinel-2 and PlanetScope satellites (Figure 6), a general overestimation of Sentinel-2 in comparison with PlanetScope was observed. Specifically, the

correlation among both satellites showed a slope term of 0.89 and an intercept value of 0.11. The relation was highly significant, with an  $R^2$  value of 0.76 and an RMSE value of 0.11.

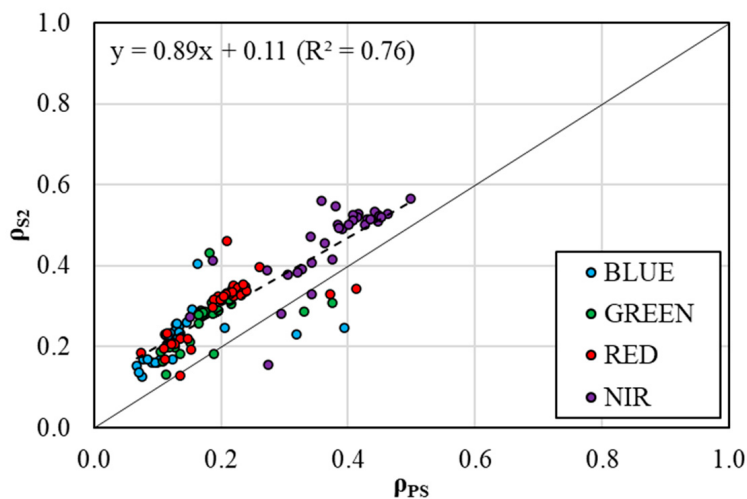


**Figure 6.** Comparison of the reflectance values from PlanetScope ( $\rho_{PS}$ ) and Sentinel-2 ( $\rho_{S2}$ ) satellites obtained in the visible (blue, green, and red) and near-infrared (NIR) spectral bands. The black dashed line represents the general trend line regression, while the black continuous line indicates the 1:1 relationship.

It was observed that the vegetation indices derived from PlanetScope and Sentinel-2 data demonstrated almost identical and consistent temporal patterns. An example of the NDVI obtained from Sentinel 2 and PlanetScope images is shown in Figure 7. All vegetation indices showed their lowest values (in absolute terms) at the beginning of the vegetative period. Vegetation indices values began to increase steadily after a few weeks, varying from Day of Year (DOY) 55–99 depending on the satellite used, indicating the start of vegetative stages (e.g., leaf development) and significant growth. The vine growth increased until reaching DOYs 130–190, corresponding to the highest growth values. From that point, the vine started to fruit, coinciding with when vegetation indices began to decrease at DOYs 205–249. A peculiarity in this case is that values rise again between DOYs 280 and 330, which corresponds to the fact that weeds have not been removed from the field. However, in absolute terms, the values calculated from Sentinel-2 and PlanetScope responded differently in the function of the evaluated vegetation index.

The major discrepancies among satellites occurred in terms of NDVI, GNDVI, NDWI, and SR (Figure 8). More specifically, NDVI derived from PlanetScope shows an average range of values from 0.11 to 0.51, while Sentinel-2 ranges between 0.09 and 0.33. GNDVI values in PlanetScope ranged from 0.19 to 0.51 during the crop cycle, whereas the values derived from Sentinel-2 varied from 0.14 to 0.34. NDWI values from PlanetScope and Sentinel-2 ranged from −0.51 to −0.19 and from −0.34 to −0.14, respectively. In the case of SR, the values derived from PlanetScope imagery during the evaluated time period ranged from 1.25 to 3.16, whereas the values obtained from Sentinel-2 varied from 1.19 to 1.98.

Lower differences among the values provided by both satellites were observed in terms of SAVI and OSAVI. Thus, SAVI values ranged from 0.10 to 0.36 when using PlanetScope images, whereas the values ranged from 0.07–0.27 when using Sentinel-2 data. Similar values were obtained for OSAVI, with values ranging from 0.09 to 0.38 and from 0.07 to 0.26 when considering PlanetScope and Sentinel-2, respectively.



**Figure 7.** Example of NDVI calculated from Sentinel2 (a) and PlanetScope (b) images acquired on 29 June 2022.

The values calculated from PlanetScope and Sentinel-2 did not show significant differences in terms of EVI, MTVI, and MSAVI, except for the last dates of the cycle, where the differences became greater. Thus, EVI, MTVI, and MSAVI from both satellites varied from 0.09 to 0.39, from 0.00 to 0.54, and from 0.57 to 0.84, respectively.

### 3.3. Detection of Clusters with YOLOv7x and Comparison with Vegetation Indices

From the comparison between the total cluster number derived from YOLOv7x and the average vegetation indexes in the field obtained for each single image and for the cumulative value, it can be observed that vegetation indexes were not able to accurately predict the cluster numbers. These results occurred both when using PlanetScope-derived vegetation indexes and when using those vegetation indexes calculated from Sentinel-2 imagery (Tables 3–5). More specifically, the lack of a significant relationship was evidenced by the low  $R^2$  values obtained, which reached a maximum of 0.23 when using Sentinel-2 imagery (NDWI and GNDVI versus cluster vine $^{-1}$  on 6 November 2022; Table 3), being even lower when PlanetScope imagery was used (maximum of 0.02 obtained for NDVI versus cluster vine $^{-1}$  on 25 May 2022; Table 4). The consideration of the cumulative values during the evaluated period did not improve the obtained results, with the  $R^2$  values of the relationships vegetation indexes versus clusters vine $^{-1}$  lower than 0.09 (Table 5).

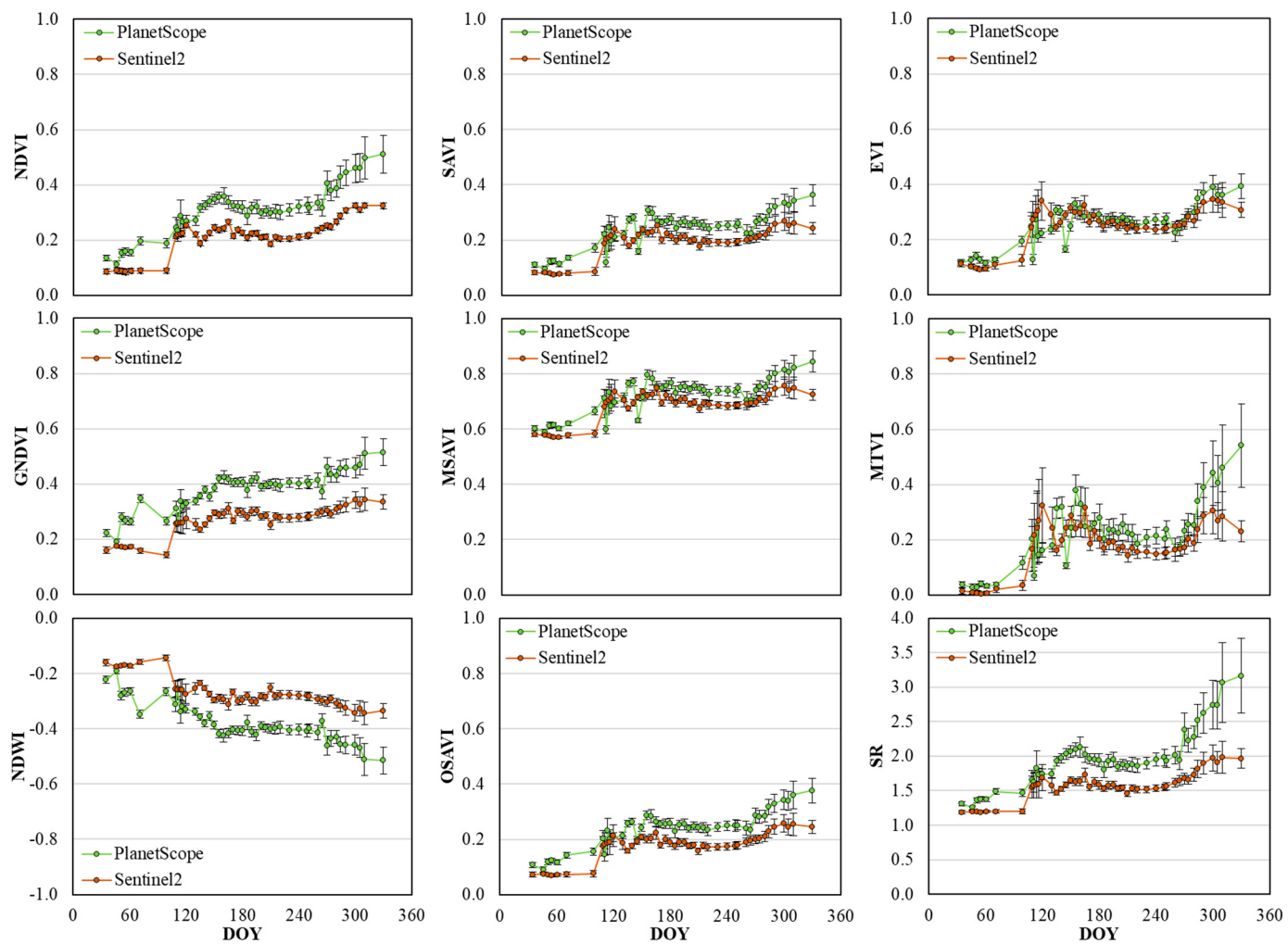


**Figure 8.** Temporal evolution of the different vegetation indexes calculated from PlanetScope and Sentinel-2 satellites (DOY: Day Of Year).

**Table 3.**  $R^2$  values obtained for the relationships between the different vegetation indexes derived from the Sentinel-2 satellite and the number of clusters for each individual date. For the meaning of the indexes, the reader is referred to the main text. The bold values evidence the maximum obtained  $R^2$  value.

Data	NDVI	SAVI	EVI	GNDVI	MSAVI	MTVI	NDWI	OSAVI	SR
4 February	0.007	0.003	$2 \times 10^{-4}$	$4 \times 10^{-6}$	0.001	0.020	$4 \times 10^{-6}$	0.006	0.007
14 February	0.013	0.013	0.005	0.021	0.008	0.014	0.021	0.023	0.031
24 February	$9 \times 10^{-4}$	0.005	0.007	0.062	0.007	0.031	0.062	0.003	0.001
1 March	0.004	0.010	0.006	0.055	0.013	$7 \times 10^{-4}$	0.055	0.007	0.004
10 April	0.090	0.096	0.096	0.052	0.098	0.107	0.052	0.093	0.089
20 April	0.110	0.114	0.116	0.108	0.115	0.109	0.108	0.112	0.105
25 April	0.118	0.122	0.124	0.106	0.123	0.119	0.106	0.120	0.113
30 April	0.125	0.129	0.128	0.120	0.129	0.121	0.120	0.127	0.120
10 May	0.002	0.002	0.003	0.001	0.002	0.004	0.001	0.002	0.002
15 May	0.039	0.043	0.059	0.008	0.045	0.063	0.008	0.041	0.040
20 May	0.011	0.015	0.027	0.020	0.016	0.014	0.020	0.013	0.011
25 May	0.009	0.024	0.021	0.028	0.029	0.011	0.028	0.015	0.009
30 May	0.005	0.008	0.015	0.010	0.009	0.011	0.010	0.006	0.005
4 June	$3 \times 10^{-4}$	$4 \times 10^{-4}$	0.002	$1 \times 10^{-4}$	$4 \times 10^{-4}$	0.001	$1 \times 10^{-4}$	$4 \times 10^{-4}$	$3 \times 10^{-4}$
9 June	0.007	0.008	0.007	0.007	0.008	0.007	0.007	0.008	0.007
14 June	0.004	0.004	0.004	0.005	0.004	0.002	0.005	0.004	0.003
19 June	0.023	0.021	0.018	0.003	0.020	0.026	0.003	0.022	0.022

**Table 3.** Cont.

Data	NDVI	SAVI	EVI	GNDVI	MSAVI	MTVI	NDWI	OSAVI	SR
24 June	0.032	0.032	0.042	0.024	0.032	0.030	0.024	0.032	0.030
29 June	$3 \times 10^{-5}$	$2 \times 10^{-4}$	$9 \times 10^{-4}$	0.010	$2 \times 10^{-4}$	$4 \times 10^{-4}$	0.010	$8 \times 10^{-5}$	$7 \times 10^{-5}$
4 July	$7 \times 10^{-6}$	$2 \times 10^{-4}$	0.003	0.006	$3 \times 10^{-4}$	0.005	0.006	$5 \times 10^{-5}$	$2 \times 10^{-5}$
9 July	0.042	0.040	0.055	0.025	0.039	0.043	0.025	0.041	0.042
14 July	0.001	$3 \times 10^{-4}$	$2 \times 10^{-4}$	0.001	$1 \times 10^{-4}$	$8 \times 10^{-8}$	$5 \times 10^{-4}$	$7 \times 10^{-4}$	$8 \times 10^{-4}$
19 July	0.038	0.033	0.043	0.020	0.031	0.035	0.020	0.036	0.036
24 July	0.038	0.033	0.022	0.059	0.031	0.017	0.059	0.036	0.037
29 July	0.003	0.001	0.004	0.005	0.001	0.010	0.005	0.002	0.003
3 August	$4 \times 10^{-4}$	$2 \times 10^{-5}$	$8 \times 10^{-4}$	0.001	$2 \times 10^{-4}$	0.001	0.001	$9 \times 10^{-5}$	$3 \times 10^{-4}$
8 August	0.003	0.001	0.005	0.001	0.001	0.004	$8 \times 10^{-4}$	0.002	0.003
13 August	0.091	0.092	0.094	0.062	0.093	0.056	0.062	0.092	0.092
28 August	$3 \times 10^{-4}$	0.003	0.001	0.011	0.005	$7 \times 10^{-4}$	0.011	0.001	$4 \times 10^{-4}$
7 September	0.006	0.002	0.011	0.022	0.001	0.020	0.022	0.004	0.006
22 September	0.023	0.053	0.050	0.040	0.061	0.040	0.040	0.038	0.023
27 September	0.006	0.001	$2 \times 10^{-4}$	0.002	$4 \times 10^{-4}$	$7 \times 10^{-4}$	0.002	0.004	0.005
2 October	$8 \times 10^{-4}$	0.005	0.007	$2 \times 10^{-4}$	0.007	0.010	$2 \times 10^{-4}$	0.002	$6 \times 10^{-4}$
7 October	$2 \times 10^{-4}$	0.002	0.003	0.001	0.003	0.001	0.001	$8 \times 10^{-5}$	$2 \times 10^{-4}$
17 October	0.010	0.022	0.026	0.029	0.026	0.022	0.029	0.015	0.010
27 October	0.044	0.064	0.068	0.058	0.068	0.067	0.058	0.052	0.044
1 November	0.114	0.132	0.133	0.147	0.135	0.123	0.147	0.122	0.112
6 November	0.114	0.220	0.211	<b>0.234</b>	0.216	0.198	<b>0.234</b>	0.223	0.217
26 November	0.013	0.027	0.019	0.047	0.032	0.023	0.047	0.019	0.015

**Table 4.**  $R^2$  values obtained for the relationships between the different vegetation indexes derived from the PlanetScope satellite and the number of clusters for each individual date. For the meaning of the indexes, the reader is referred to the main text. The bold value evidences the maximum obtained  $R^2$  value.

Date	NDVI	SAVI	EVI	GNDVI	MSAVI	MTVI	NDWI	OSAVI	SR
4 February	0.002	0.001	0.001	$3 \times 10^{-4}$	0.001	0.002	$3 \times 10^{-4}$	0.002	0.002
15 February	0.001	0.002	0.001	0.001	0.002	0.003	0.001	0.001	0.001
20 February	0.002	0.002	0.001	0.003	0.002	$4 \times 10^{-4}$	0.003	0.002	0.002
24 February	0.003	$2 \times 10^{-4}$	$1 \times 10^{-4}$	$1 \times 10^{-4}$	$3 \times 10^{-6}$	0.003	$1 \times 10^{-4}$	0.001	0.002
2 March	0.002	0.005	0.005	0.001	0.006	0.004	0.001	0.003	0.002
12 March	0.007	0.010	0.009	0.007	0.010	0.006	0.007	0.008	0.007
9 April	0.005	0.005	0.005	0.002	0.004	0.006	0.002	0.005	0.005
19 April	0.008	0.009	0.009	0.010	0.009	0.008	0.010	0.009	0.008
21 April	0.006	0.002	0.002	0.003	0.002	0.004	0.003	0.004	0.006
24 April	0.007	0.007	0.007	0.007	0.008	0.007	0.007	0.007	0.006
26 April	0.010	0.011	0.010	0.011	0.011	0.010	0.011	0.010	0.010
10 May	$3 \times 10^{-6}$	$3 \times 10^{-4}$	0.001	0.003	$4 \times 10^{-4}$	$2 \times 10^{-5}$	0.003	$7 \times 10^{-5}$	$6 \times 10^{-6}$
15 May	0.005	0.006	0.007	0.006	0.007	0.006	0.006	0.006	0.005
20 May	0.006	0.006	0.009	0.001	0.006	0.007	0.001	0.006	0.006
25 May	<b>0.022</b>	0.019	0.018	0.016	0.018	0.018	0.016	0.021	0.021
4 June	0.004	0.003	0.003	0.002	0.002	0.003	0.002	0.003	0.004
9 June	$7 \times 10^{-7}$	$2 \times 10^{-5}$	$9 \times 10^{-6}$	$9 \times 10^{-5}$	$4 \times 10^{-5}$	$7 \times 10^{-5}$	$9 \times 10^{-5}$	$3 \times 10^{-6}$	$5 \times 10^{-8}$
14 June	0.003	0.002	0.002	0.003	0.002	0.001	0.003	0.002	0.002
19 June	$1 \times 10^{-5}$	$8 \times 10^{-6}$	$2 \times 10^{-8}$	$2 \times 10^{-7}$	$2 \times 10^{-5}$	$2 \times 10^{-5}$	$2 \times 10^{-7}$	$1 \times 10^{-7}$	$5 \times 10^{-6}$
29 June	0.002	0.001	0.001	$3 \times 10^{-4}$	0.001	0.001	$3 \times 10^{-4}$	0.001	0.001
4 July	0.019	0.018	0.017	0.020	0.017	0.015	0.020	0.019	0.019
9 July	0.006	0.005	0.004	0.005	0.005	0.004	0.005	0.006	0.006
14 July	0.010	0.007	0.008	0.007	0.007	0.007	0.007	0.009	0.009
19 July	0.004	0.003	0.003	0.003	0.003	0.002	0.003	0.004	0.004
24 July	0.007	0.005	0.006	0.006	0.005	0.004	0.006	0.006	0.007
29 July	0.003	0.001	0.001	$4 \times 10^{-4}$	0.001	0.001	$4 \times 10^{-4}$	0.002	0.003
3 August	0.010	0.007	0.006	0.008	0.006	0.006	0.008	0.009	0.009
8 August	0.001	$4 \times 10^{-4}$	$4 \times 10^{-4}$	0.001	$3 \times 10^{-4}$	$2 \times 10^{-4}$	0.001	0.001	0.001

**Table 4.** Cont.

Date	NDVI	SAVI	EVI	GNDVI	MSAVI	MTVI	NDWI	OSAVI	SR
18 August	0.007	0.004	0.004	0.003	0.003	0.003	0.003	0.006	0.006
28 August	0.010	0.007	0.010	0.009	0.007	0.006	0.009	0.009	0.009
6 September	0.003	0.001	0.002	0.001	0.001	0.001	0.001	0.002	0.003
8 September	0.010	0.006	0.006	0.006	0.005	0.005	0.006	0.008	0.009
17 September	0.021	0.015	0.016	0.008	0.013	0.016	0.008	0.020	0.020
22 September	0.008	0.001	0.001	0.004	0.001	0.001	0.004	0.004	0.007
27 September	0.008	0.005	0.005	0.006	0.004	0.005	0.006	0.007	0.007
1 October	0.010	0.006	0.005	0.009	0.004	0.004	0.009	0.008	0.009
7 October	0.001	$2 \times 10^{-4}$	$4 \times 10^{-4}$	0.001	$4 \times 10^{-4}$	$4 \times 10^{-4}$	0.001	$2 \times 10^{-5}$	$2 \times 10^{-4}$
11 October	$2 \times 10^{-4}$	$6 \times 10^{-5}$	$3 \times 10^{-5}$	$2 \times 10^{-5}$	$2 \times 10^{-4}$	$1 \times 10^{-4}$	$2 \times 10^{-5}$	$2 \times 10^{-5}$	$1 \times 10^{-4}$
17 October	0.017	0.018	0.006	0.006	0.018	0.008	0.006	0.018	0.014
27 October	$1 \times 10^{-4}$	0.001	0.001	$2 \times 10^{-5}$	0.001	0.001	$2 \times 10^{-5}$	$2 \times 10^{-5}$	0.014
1 November	0.001	$7 \times 10^{-6}$	$1 \times 10^{-4}$	$4 \times 10^{-4}$	$8 \times 10^{-5}$	$2 \times 10^{-4}$	$4 \times 10^{-4}$	$2 \times 10^{-4}$	$2 \times 10^{-4}$
6 November	$2 \times 10^{-6}$	0.001	0.001	$6 \times 10^{-5}$	0.001	0.001	$6 \times 10^{-5}$	$1 \times 10^{-4}$	$1 \times 10^{-5}$
26 November	0.008	0.005	0.002	0.007	0.004	0.002	0.007	0.007	0.005

**Table 5.**  $R^2$  values obtained for the relationships between the different vegetation indexes derived from Sentinel-2 and PlanetScope satellites and the number of clusters for the cumulative period of the study. For the meaning of the indexes, the reader is referred to the main text.

Platform	NDVI	SAVI	EVI	GNDVI	MSAVI	MTVI	NDWI	OSAVI	SR
Sentinel-2	0.059	0.073	0.082	0.076	0.078	0.083	0.076	0.065	0.066
PlanetScope	0.001	$2 \times 10^{-5}$	$2 \times 10^{-6}$	$3 \times 10^{-4}$	$2 \times 10^{-6}$	$6 \times 10^{-7}$	$3 \times 10^{-4}$	0.001	0.001

#### 4. Discussion

Object detection models based on YOLOv7x showed moderate accuracy in grape cluster detection, with metrics such as mAP and F1 score reaching acceptable values. However, it is necessary to reduce false positives and improve the precise localization of clusters. This suggests that, although the model is able to detect most of the grape clusters present in the images, it also makes errors by detecting incorrect objects. Compared to other YOLO versions, such as YOLOv5s and YOLOv3-spp, YOLOv7x demonstrated better accuracy [65]. For example, ref. [46] compared the precision and recall metrics of YOLOv7x, YOLOv7-E6, and YOLOv8, observing that YOLOv7x demonstrated greater consistency under different UAV flight configurations, with RMSE values of 0.75 and 0.78 grape clusters per vine. The combination of UAV images with advanced algorithms, such as YOLOv7x, significantly improved detection compared to the exclusive use of satellite data, which could lack enough spatial resolution to perform grape cluster estimations. In fact, the pixel sizes of the satellite images considered (Sentinel-2 and PlanetScope), do not account only for the presence of grape clusters but include all features included within the pixels of 10 m and 3 m. In this sense, the utilization of satellite images with a higher spatial resolution, such as those obtained from WorldView satellites or even from UAVs, could allow for a more accurate identification of the elements of the images. Additionally, the main purpose of vegetation indices was to represent vegetation vigor and health, rather than directly indicating yield parameters.

Despite the overall good performance of YOLOv7x, its detection capacity is limited by false positives and difficulties in identifying clusters partially covered or under adverse lighting conditions. A possible improvement would be the use of image preprocessing techniques, such as lighting normalization, and increasing the dataset for algorithm training.

The results obtained in this study highlight the importance of combining various remote sensing data sources to optimize grape cluster detection in vineyards, thus contribut-

ing to precision agriculture. The comparison between UAV, Sentinel-2, and PlanetScope images shows that, although UAVs provide superior spatial resolution, the satellite data from Sentinel-2 and PlanetScope offer complementary advantages in terms of radiometric stability and temporal coverage.

Specifically, UAVs excel in their ability to detect fine details, such as grape clusters, thanks to their high spatial resolution, which is crucial for small plots and detailed studies [66–69]. However, their lower radiometric stability and associated costs limit their application to larger scales or prolonged studies. On the other hand, Sentinel-2, with its greater radiometric stability and revisit frequency, is more suitable for large-scale and long-term studies, as evidenced by previous research highlighting its efficiency in monitoring crop growth and health over larger areas [52,70,71].

The inclusion of PlanetScope images, which have high temporal resolution and intermediate spatial resolution, allowed for capturing detailed variations within plots. However, higher variability in reflectance values was observed, as noted in [72,73]. PlanetScope's superior results are due to both its higher geometric resolution, which better aligns with the study areas, and its ability to adjust pixel purity, which measures the degree of homogeneity with respect to the target crop [70]. This suggests that PlanetScope images could be more useful in studies requiring detailed observations at small scales, where precise radiometric adjustments are needed [70,71]. Overall, the synergistic combination of high-resolution PlanetScope data with medium-resolution Sentinel-2 data outperforms the predictive performance of each dataset separately, due to the combination of spatial and spectral information from both sources [71–74]. Thus, the use of multi-scale models is recommended to optimize predictions.

Regarding yield estimation, higher correlation values were observed in Sentinel-2 data compared to PlanetScope, which is consistent with other studies comparing both datasets [63]. Although PlanetScope data had higher temporal and spatial resolution, it had lower radiometric resolution than Sentinel-2 data. The lack of two additional red-edge and SWIR bands in PlanetScope data may also be a factor influencing these results [63]. Nevertheless, PlanetScope's near-daily image frequency provides opportunities to improve prediction accuracy and promote digital agriculture for crop modeling [75]. Currently, Sentinel-2 images are considered the most suitable for field-level yield estimation [76]. The higher standard deviation in PlanetScope suggests that its higher spatial resolution allows it to capture finer differences in areas with less dense vegetation or mixed with bare soil. Conversely, Sentinel, with its lower but more uniform resolution, offers more consistent results for large-scale studies.

The vegetation indices used, such as NDVI, SAVI, EVI, GNDVI, MSAVI, MTVI, NDWI, OSAVI, and SR; are designed to assess vegetation vigor and overall cover but do not capture specific details like fruit clusters, which often have spectral characteristics similar to surrounding foliage or are partially obscured by the canopy.

This is because these indices are designed to assess overall vegetation cover but cannot accurately differentiate grape clusters from surrounding vegetation, which often share similar spectral characteristics or are partially covered by the canopy. Our results showed an increase in indices in autumn, possibly related to weed growth on the ground, consistent with other studies [66,77], where this increase is also related to orchard water consumption depending on both irrigation practices and pedoclimatic conditions [78–80].

In related studies, ground-based imagery is commonly used for grape bunch detection [29], while others used UAV imagery and NDVI to identify live and dry vines [30]. Some works also compared the performance of different satellite image sources, such as WorldView, PlanetScope, and Sentinel-2, concluding that high-resolution imagery, such as WorldView (i.e., <1 m), is essential for detecting small features [81]. This could explain why

neither Sentinel nor PlanetScope imagery has shown any relationship with the grape cluster number in the present study. Other studies focused on yield prediction using vegetation indices but without performing detection on the fruit [31]. This limitation of the vegetation indexes (such as NDVI) for deriving yield parameters has also been reported by other authors. In particular, refs. [31,32] observed that vegetation indexes (e.g., NDVI, EVI, and SAVI) showed inconsistency in yield prediction depending on factors such as the amount of reference data, study area, climate, cloud cover, atmospheric conditions, and inadequate calibration affect the accuracy of these measurements.

For future research, the use of LiDAR data is proposed, as it could provide three-dimensional information about the canopy and clusters, improving detection accuracy [74]. The combination of LiDAR data with multispectral images and advanced object detection models could open new opportunities for automatic yield estimation in vineyards.

Finally, although this study focused on grape cluster detection, it would be interesting to apply this approach to other fruit crops facing similar challenges in terms of automatic fruit detection.

These results demonstrate that although PlanetScope offers higher spatial resolution, Sentinel-2's reflectance values show greater consistency, which could translate into better capability for temporal or large-area studies. On the other hand, PlanetScope, due to its higher variability in bands, might be more suitable for applications requiring detailed observation of smaller areas but with a greater need for radiometric adjustment.

This difference in bands is critical when selecting which platform to use based on the study's objective. Sentinel-2 is ideal for more homogeneous and long-term monitoring, while PlanetScope is preferable when very fine spatial resolution and detailed analysis of small agricultural plots are required.

## 5. Conclusions

This study provides a detailed comparison between the use of UAV images and satellite images from Sentinel-2 and PlanetScope for the automatic detection of grape clusters in vineyards using the YOLOv7x model. The results of training the YOLOv7x model demonstrated moderate accuracy in grape cluster detection, with acceptable performance in metrics such as precision and recall, but with room for improvement in reducing false positives. It is concluded that vegetation indices alone are not sufficient to accurately predict the presence of clusters, as they are designed to assess vegetative vigor and biomass rather than detect specific objects such as grape clusters. However, it was observed that PlanetScope, despite its high spatial resolution, did not achieve as stable a correlation with grape cluster detection data compared to Sentinel-2.

It is observed that classical vegetation indices, such as NDVI, SAVI, EVI, GNDVI, MSAVI, MTVI, NDWI, OSAVI, and SR from both Sentinel-2 and PlanetScope, did not show a significant correlation with grape cluster detection. These indices, commonly used to assess plant vigor and health, do not effectively differentiate the clusters due to their spectral similarities with the surrounding foliage or their partial occlusion under the plant canopy.

In terms of data sources comparison, images obtained from UAVs offer a significant advantage in terms of spatial resolution, allowing for a more detailed identification of grape clusters. The detailed comparison of reflectance bands and vegetation indices between Sentinel-2 and PlanetScope reveals that, although PlanetScope offers a higher spatial resolution of 3 m, Sentinel-2 (10 m) shows greater radiometric stability and temporal consistency. This makes it more suitable for vegetation studies over large areas and prolonged temporal analyses, while PlanetScope could be more useful in studies where fine spatial resolution is of greater importance.

The integration of UAV images with advanced deep learning models such as YOLOv7x significantly enhances the detection of grape clusters by leveraging the superior spatial resolution of UAV data. This combination enables more accurate identification of clusters, reducing occlusion issues and increasing the precision of detection models. UAVs offer flexibility in data collection, allowing for timely and targeted surveys that can be adapted to specific vineyard conditions. This synergy between UAV imagery and deep learning provides a robust framework for addressing the limitations of satellite data and vegetation indices, ultimately supporting more precise, data-driven decision-making in vineyard management.

Finally, this study suggests that the most effective approach for detecting grape clusters in vineyards combines the use of UAV images to capture specific details, along with multispectral satellite data such as Sentinel-2 and PlanetScope, complemented by advanced object detection models like YOLOv7x. This approach allows for optimizing productivity and improving sustainability in vineyard management, providing more precise and effective tools for data-driven decision-making.

**Author Contributions:** Conceptualization, A.M.C.-A. and J.M.R.-C.; methodology, A.M.C.-A., N.F., G.S. and P.F.-G.; validation, A.M.C.-A., N.F. and G.S.; formal analysis, A.M.C.-A., N.F., G.S., S.F., H.P., C.R.-O., P.F.-G. and J.M.R.-C.; data curation, A.M.C.-A., N.F., G.S., P.F.-G. and J.M.R.-C.; writing—original draft preparation, A.M.C.-A. and J.M.R.-C.; writing—review and editing, P.F.-G., S.F., H.P. and C.R.-O.; supervision, S.F., H.P., C.R.-O. and J.M.R.-C.; funding acquisition, H.P. and C.R.-O. All authors have read and agreed to the published version of the manuscript.

**Funding:** The study was funded by the research grant from Miguel Hernández University 79SH0010RP “Análisis de imágenes en agricultura de precisión para cultivos de interés local”.

**Data Availability Statement:** The data presented in this study are available on request from the corresponding author due to privacy.

**Conflicts of Interest:** The authors declare no conflicts of interest.

## References

- Bhakta, I.; Phadikar, S.; Majumder, K. State-of-the-art technologies in precision agriculture: A systematic review. *J. Sci. Food Agric.* **2019**, *99*, 4878–4888. [[CrossRef](#)]
- Kendall, H.; Clark, B.; Li, W.; Jin, S.; Jones, G.D.; Chen, J.; Taylor, J.; Li, Z.; Frewer, L.J. Precision agriculture technology adoption: A qualitative study of small-scale commercial “family farms” located in the North China Plain. *Precis. Agric.* **2022**, *23*, 319–351. [[CrossRef](#)]
- Soumitra, N. A vision of precision agriculture: Balance between agricultural sustainability and environmental stewardship. *Agron. J.* **2023**, *116*, 1126–1143.
- Liu, J.; Xiang, J.; Jin, Y.; Liu, R.; Yan, J.; Wang, L. Boost precision agriculture with unmanned aerial vehicle remote sensing and edge intelligence: A survey. *Remote Sens.* **2021**, *13*, 4387. [[CrossRef](#)]
- Leroux, C.; Jones, H.; Pichon, L.; Guillaume, S.; Lamour, J.; Taylor, J.; Naud, O.; Crestey, T.; Lablee, J.-L.; Tisseyre, B. GeoFIS: An open-source decision-support tool for precision agriculture data. *Agriculture* **2018**, *8*, 73. [[CrossRef](#)]
- Guo, J.; Li, X.; Li, Z.; Hu, L.; Yang, G.; Zhao, C.; Fairbairn, D.; Watson, D.; Ge, M. Multi-GNSS precise point positioning for precision agriculture. *Precis. Agric.* **2018**, *19*, 895–911. [[CrossRef](#)]
- Wolfert, S.; Ge, L.; Verdouw, C.; Bogaardt, M.-J. Big data in smart farming—A review. *Agric. Syst.* **2017**, *153*, 69–80. [[CrossRef](#)]
- Toscano, F.; Fiorentino, C.; Capece, N. Unmanned Aerial Vehicle for Precision Agriculture: A Review. *IEEE Access* **2024**, *12*, 69188–69205. [[CrossRef](#)]
- Adewusi, A.O. AI in precision agriculture: A review of technologies for sustainable farming practices. *World J. Adv. Res. Rev.* **2024**, *21*, 2276–2285. [[CrossRef](#)]
- Krishna, K.R. *Agricultural Drones: A Peaceful Search*; CRC Press: Boca Raton, FL, USA, 2018.
- Marinello, F.; Pezzuolo, A.; Chiumenti, A.; Sartori, L. Technical analysis of unmanned aerial vehicles (drones) for agricultural applications. *Eng. Rural Dev.* **2016**, *15*, 870–875.
- Veroustraete, F. The rise of drones in agriculture. *EC Agric.* **2015**, *2*, 325–327.

13. Daponte, P.; Vito, L.; Glielmo, L.; Iannelli, L.; Liuzza, D.; Picariello, F.; Silano, G. A review on the use of drones for precision agriculture. *IOP Conf. Ser. Earth Environ. Sci.* **2019**, *275*, 012022. [[CrossRef](#)]
14. Furnitto, N.; Ramírez-Cuesta, J.M.; Sottosanti, G.; Longo, D.; Schillaci, G.; Failla, S. Potentiality of Multispectral Vegetation Indexes for Evaluating the Influence of the Sowing Technique on Durum Wheat Cultivation Density. In Proceedings of the Safety, Health and Welfare in Agriculture and Agro-Food Systems, Ragusa, Italy, 6–9 September 2023; pp. 313–321.
15. Manfreda, S. On the use of unmanned aerial systems for environmental monitoring. *Remote Sens.* **2018**, *10*, 641. [[CrossRef](#)]
16. Payares, A.; Tarquis, A.H.; Peraló, R.; Canó, J.; Cámaras, J.; Gómez del Campo, M. Multispectral and thermal sensors on board UAVs for heterogeneity in Merlot vineyard detection: Contribution to zoning maps. *Remote Sens.* **2023**, *15*, 4024. [[CrossRef](#)]
17. Pérez-Zavala, R.; Torres-Torriti, M.; Cheein, F.A.; Troni, G. A pattern recognition strategy for the visual detection of grape clusters in vineyards. *Comput. Electron. Agric.* **2018**, *151*, 136–149. [[CrossRef](#)]
18. Sozzi, M.; Cantalamessa, S.; Cogato, A.; Kayad, A.; Marinello, F. Automatic cluster detection in white grape varieties using YOLOv3, YOLOv4, and YOLOv5 deep learning algorithms. *Agronomy* **2022**, *12*, 319. [[CrossRef](#)]
19. Squeri, C.; Poni, S.; Matese, A.; Gatti, M. Comparison and verification of the terrain of different remote and proximal sensing platforms to characterize variability in a hedgerow-grown vineyard. *Remote Sens.* **2021**, *13*, 2056. [[CrossRef](#)]
20. Cogato, A.; Meggio, F.; Collins, C.; Marinello, F. Sentinel-2 medium-resolution multispectral data to assess damage and recovery time from late frosts in vineyards. *Remote Sens.* **2020**, *12*, 1896. [[CrossRef](#)]
21. Payne, A.B.; Walsh, K.B.; Subedi, P.P.; Jarvis, D. Estimation of mango crop yield using image analysis—Segmentation method. *Comput. Electron. Agric.* **2013**, *91*, 57–64. [[CrossRef](#)]
22. Robson, A.; Rahman, M.M.; Muir, J. Using worldview satellite imagery to map yield in avocado (*Persea americana*): A case study in Bundaberg, Australia. *Remote Sens.* **2017**, *9*, 1223. [[CrossRef](#)]
23. Shi, R.; Li, T.; Yamaguchi, Y. An attribution-based pruning method for real-time mango detection with YOLO network. *Comput. Electron. Agric.* **2020**, *169*. [[CrossRef](#)]
24. Ballesteros, R.; Intrigliolo, D.S.; Ortega, J.F.; Ramírez-Cuesta, J.M.; Buesa, I.; Moreno, M.A. Vineyard yield estimation by combining remote sensing, computer vision and artificial neural network techniques. *Precis. Agric.* **2020**, *21*, 1242–1262. [[CrossRef](#)]
25. Wang, Y.; Yi, Y.; Wang, X.-F.; Chen, J.; Li, X. Fig fruit recognition method based on YOLOv4 deep learning. In Proceedings of the 2021 18th International Conference on Electrical Engineering, Electronics, Computer, Telecommunications and Information Technology: Smart Electrical System and Technology, ECTI-CON, Bangkok, Thailand, 24–26 March 2021; pp. 303–306. [[CrossRef](#)]
26. Íñiguez, R.; Gutiérrez, S.; Poblete-Echeverría, C.; Hernández, I.; Barrio, I.; Tardáguila, J. Deep learning modelling for non-invasive grape bunch detection under diverse occlusion conditions. *Comput. Electron. Agric.* **2024**, *226*, 109421. [[CrossRef](#)]
27. Jiménez, A.; Ceres, R.; Pons, J.L. A study of computer vision methods for locating fruit on trees. *Trans. ASAE* **2000**, *43*, 1911–1920. [[CrossRef](#)]
28. Xiong, J.; Lin, R.; Liu, Z.; He, Z.; Tang, L.; Yang, Z.; Zou, X. The recognition of groups of lychee and the calculation of the collection point in a natural night-time environment. *Biosyst. Eng.* **2018**, *166*, 44–57. [[CrossRef](#)]
29. Wang, W.; Shi, Y.; Liu, W.; Che, Z. An unstructured orchard grape detection method utilizing YOLOv5s. *Agriculture* **2024**, *14*, 262. [[CrossRef](#)]
30. Gavrilović, M.; Jovanović, D.; Božović, P.; Benka, P.; Govendarica, M. Vineyard Zoning and Vine Detection Using Machine Learning in Unmanned Aerial Vehicle Imagery. *Remote Sens.* **2024**, *16*, 584. [[CrossRef](#)]
31. Sun, L.; Gao, F.; Anderson, M.C.; Kustas, W.P.; Alsina, M.M.; Sanchez, L.; Sams, B.; McKee, L.; Dulaney, W.; White, W.A.; et al. Daily Mapping of 30 m LAI and NDVI for Grape Yield Prediction in California Vineyards. *Remote Sens.* **2017**, *9*, 317. [[CrossRef](#)]
32. Guan, S.; Fukami, K.; Matsunaka, H.; Okami, M.; Tanaka, R.; Nakano, H.; Sakai, T.; Nakano, K.; Ohdan, H.; Takahashi, K. Assessing Correlation of High-Resolution NDVI with Fertilizer Application Level and Yield of Rice and Wheat Crops Using Small UAVs. *Remote Sens.* **2019**, *11*, 112. [[CrossRef](#)]
33. Labus, M.P.; Nielsen, G.A.; Lawrence, R.L.; Engel, R.; Long, D.S. Wheat Yield Estimates Using Multi-Temporal NDVI Satellite Imagery. *Int. J. Remote Sens.* **2002**, *23*, 4169–4180. [[CrossRef](#)]
34. Vannoppen, A.; Gobin, A. Estimating Farm Wheat Yields from NDVI and Meteorological Data. *Agronomy* **2021**, *11*, 946. [[CrossRef](#)]
35. Karkauskaite, P.; Tagesson, T.; Fensholt, R. Evaluation of the Plant Phenology Index (PPI), NDVI and EVI for Start-of-Season Trend Analysis of the Northern Hemisphere Boreal Zone. *Remote Sens.* **2017**, *9*, 485. [[CrossRef](#)]
36. Jaafar, H.H.; Zurayk, R.; King, C.; Ahmad, F.; Al-Outa, R. Impact of the Syrian Conflict on Irrigated Agriculture in the Orontes Basin. *Int. J. Water Resour. Dev.* **2015**, *31*, 436–449. [[CrossRef](#)]
37. Redmon, J.; Divvala, S.; Girshick, R.; Farhadi, A. You only look once: Unified, real-time object detection. In Proceedings of the IEEE Conference on Computer Vision and Pattern Recognition, Las Vegas, NV, USA, 26 June–1 July 2016.
38. Santos, T.T.; de Souza, L.L.; dos Santos, A.A.; Ávila, S. Detection, segmentation and tracking of grapes using deep neural networks and three-dimensional association. *Comput. Electron. Agric.* **2020**, *170*, 105247. [[CrossRef](#)]
39. Liu, G.; Nouaze, J.T.; Kim, J.P. A robust algorithm for tomato detection based on YOLOv3. *Sensors* **2020**, *20*, 2145. [[CrossRef](#)]

40. Dong, X.; Lan, J.; Zhu, Y. Method for identifying the collection position of lychee based on YOLOv5 and PSPNet. *Remote Sens.* **2022**, *14*, 2004.
41. Regulatory Council of the Protected Designation of Origin Vinalopó Bagged Table Grapes. Available online: <https://uva-vinalopo.org> (accessed on 3 October 2024).
42. General Directorate of Rural Development and Common Agricultural Policy. *Specifications of the Protected Designation of Origin Vinalopó Bagged Table Grapes*; Ciutat Administrativa 9 d’Octubre: Valencia, Italy, 2015.
43. Koirala, A.; Jha, M.; Bodapati, S.; Mishra, A.; Chetty, G.; Sahu, P.K.; Mohanty, S.; Padhan, T.K.; Mattoo, J.; Hukkoo, A. Deep learning for real-time malaria parasite detection and counting using YOLO-mp. *IEEE Access* **2022**, *10*, 102157–102172. [CrossRef]
44. Muhsashin, M.N.I.; Stefanie, A. Klasifikasi penyakit mata berdasarkan citra fundus menggunakan YOLO V8. *J. Mahasiswa Tek. Inform.* **2023**, *7*, 1363–1368. [CrossRef]
45. Badeka, E.; Karapatzak, E.; Karampatea, A.; Bouloumpasi, E.; Kalathas, I.; Lytridis, C.; Tziolas, E.; Tsakalidou, V.N.; Kaburlasos, V.G. A deep learning approach for precision viticulture: Assessing grape maturity via YOLOv7. *Sensors* **2023**, *23*, 8126. [CrossRef]
46. Codes-Alcaraz, A.; Puerto-Molina, H.; Rocamora-Osorio, C.; Furnitto, N.; Failla, S.; Ramírez-Cuesta, J.M. Deciphering the role of UAV flight height and sensor inclination in the prediction of table grape production through computer vision techniques. In Proceedings of the IEEE International Workshop on Metrology for Agriculture and Forestry, MetroAgriFor 2024, Padua, Italy, 29–31 October 2024. Proceedings, 2024, in press.
47. Vijayasekaran, D. SEN2-AGRI—Crop type mapping pilot study using Sentinel-2 satellite imagery in India. *Int. Arch. Photogramm. Remote Sens. Spatial Inf. Sci.* **2019**, *XLII-3/W6*, 175–180. [CrossRef]
48. Sentinel User Handbook and Exploitation Tools (SUHET). Sentinel-2 user handbook (Issue: 1, Revision: 2). European Space Agency Standard Document 2015. Available online: [https://sentinel.esa.int/documents/247904/685211/Sentinel-2\\_User\\_Handbook](https://sentinel.esa.int/documents/247904/685211/Sentinel-2_User_Handbook) (accessed on 5 December 2024).
49. Planet Labs. A Bigger Crayon Box with SuperDove’s 8 Spectral Bands. In *Manual Planet*; Planet Labs: San Francisco, CA, USA, 2024.
50. Planet Team. Planet Application Program Interface. In *Space for Life on Earth*; Planet Team: San Francisco, CA, USA, 2017.
51. Waltuch, M.; Cameron, E.; Lafframboise, A.; Zeiler, M. *Exploring ArcObjects Vol. 1—Applications and Cartography*; ESRI Press: Redlands, CA, USA, 2001.
52. Farmonov, N.; Amankulova, K.; Szatmári, J.; Urinov, J.; Narmanov, Z.; Nosirov, J.; Mucsi, L. Combining PlanetScope and Sentinel-2 Images with Environmental Data for Improved Wheat Yield Estimation. *Int. J. Digit. Earth* **2023**, *16*, 847–867. [CrossRef]
53. Amankulova, K.; Farmonov, N.; Abdelsamei, E.; Szatmári, J.; Khan, W.; Zhran, M.; Rustamov, J.; Akhmedov, S.; Sarimsakov, M.; Mucsi, L. A Novel Fusion Method for Soybean Yield Prediction Using Sentinel-2 and PlanetScope Imagery. *Remote Sens.* **2024**, *17*, 13694–13707. [CrossRef]
54. Angelini, R.; Angelats, E.; Luzi, G.; Ribas, F.; Masiero, A. Shoreline extraction methods from Sentinel-2 and PlanetScope images. *Int. Arch. Photogramm. Remote Sens. Spatial Inf. Sci.* **2024**, *XLVIII-1-2024*, 1–6. [CrossRef]
55. Furnitto, N.; Ramírez-Cuesta, J.M.; Sottosanti, G.; Schillaci, G.; Failla, S. Appraising the use of remote and proximal platforms for wheat biomass estimation from multispectral imagery. In Proceedings of the International Mid-Term Conference 2024 of the Italian Association of Agricultural Engineering (AIIA), Padova, Italy, 17–19 June 2024; Lecture Notes in Civil Engineering (LNCE). Springer Nature: Cham, Switzerland, 2025. in press.
56. Rouse, J.W.; Haas, R.H.; Schell, J.A.; Deering, D.W. Monitoring vegetation systems in the Great Plains with ERTS. In Proceedings of the Third Earth Resources Technology Satellite—1 Symposium, Washington, DC, USA, 10–14 December 1973. NASA SP-351.
57. Gitelson, A.A.; Kaufman, Y.J.; Merzlyak, M.N. Use of a green channel in remote sensing of global vegetation from EOS-MODIS. *Remote Sens. Environ.* **1996**, *58*, 289–298. [CrossRef]
58. Huete, A.R. A Soil-Adjusted Vegetation Index (SAVI). *Remote Sens. Environ.* **1988**, *25*, 295–309. [CrossRef]
59. Qi, J.; Chehbouni, A.; Huete, A.R.; Kerr, Y.H.; Sorooshian, S. A Modified Soil Adjusted Vegetation Index. *Remote Sens. Environ.* **1994**, *48*, 119–126. [CrossRef]
60. Haboudane, D. Hyperspectral Vegetation Indices and Novel Algorithms for Predicting Green LAI of Crop Canopies: Modeling and Validation in the Context of Precision Agriculture. *Remote Sens. Environ.* **2004**, *90*, 337–352. [CrossRef]
61. Huete, A.R.; Liu, H.Q.; Batchily, K.; van Leeuwen, W. A comparison of vegetation indices over a global set of TM images for EOS-MODIS. *Remote Sens. Environ.* **1997**, *59*, 440–451. [CrossRef]
62. Rondeaux, G.; Steven, M.; Baret, F. Optimization of soil-adjusted vegetation indices. *Remote Sens. Environ.* **1996**, *55*, 95–107. [CrossRef]
63. Jordan, C.F. Derivation of leaf-area index from quality of light on the forest floor. *Ecology* **1969**, *50*, 663–666. [CrossRef]
64. McFeeters, S.K. The use of the normalized difference water index (NDWI) in the delineation of open water features. *Int. J. Remote Sens.* **1996**, *17*, 1425–1432. [CrossRef]

65. Wu, D.; Jiang, S.; Zhao, E.; Liu, Y.; Zhu, H.; Wang, W.; Wang, R. Detection of *Camellia oleifera* fruit in complex scenes by using YOLOv7 and data augmentation. *Appl. Sci.* **2022**, *12*, 11318. [[CrossRef](#)]
66. Ortuaní, B.; Mayer, A.; Bianchi, D.; Sona, G.; Crema, A.; Modina, D.; Bolognini, M.; Brancadoro, L.; Boschetti, M.; Facchi, A. Effectiveness of management zones delineated from UAV and Sentinel-2 data for precision viticulture applications. *Remote Sens.* **2024**, *16*, 635. [[CrossRef](#)]
67. Khaliq, A.; Comba, L.; Biglia, A.; Ricauda Aimonino, D.; Chiaberge, M.; Gay, P. Comparison of satellite and UAV-based multispectral imagery for vineyard variability assessment. *Remote Sens.* **2019**, *11*, 436. [[CrossRef](#)]
68. Matese, A.; Toscano, P.; Di Gennaro, S.; Genesio, L.; Vaccari, F.; Primicerio, J.; Belli, C.; Zaldei, A.; Bianconi, R.; Gioli, B. Intercomparison of UAV, aircraft, and satellite remote sensing platforms for precision viticulture. *Remote Sens.* **2015**, *7*, 2971–2990. [[CrossRef](#)]
69. Di Gennaro, S.F.; Toscano, P.; Gatti, M.; Poni, S.; Berton, A.; Matese, A. Spectral comparison of UAV-based hyper and multispectral cameras for precision viticulture. *Remote Sens.* **2022**, *14*, 449. [[CrossRef](#)]
70. Lucero, M.F.; Hernández, C.M.; Carcedo, A.J.P.; Zajdband, A.; Guillevic, P.C.; Houborg, R.; Hamilton, K.; Ciampitti, I.A. Enhancing alfalfa biomass prediction: An innovative framework using remote sensing data. *Remote Sens.* **2024**, *16*, 3379. [[CrossRef](#)]
71. Wang, Z.; Wu, W.; Liu, H. Spatial estimation of soil organic carbon content utilizing PlanetScope, Sentinel-2, and Sentinel-1 data. *Remote Sens.* **2024**, *16*, 3268. [[CrossRef](#)]
72. Manivasagam, V.S.; Sadeh, Y.; Kaplan, G.; Bonfil, D.J.; Rozenstein, O. Studying the feasibility of assimilating Sentinel-2 and PlanetScope imagery into the SAFY crop model to predict within-field wheat yield. *Remote Sens.* **2021**, *13*, 2395. [[CrossRef](#)]
73. Huang, J.; Ma, H.; Sedano, F.; Lewis, P.; Liang, S.; Wu, Q.; Su, W.; Zhang, X.; Zhu, D. Evaluation of regional estimates of winter wheat yield by assimilating three remotely sensed reflectance datasets into the coupled WOFOST-PROSAIL model. *Eur. J. Agron.* **2019**, *102*, 1–13. [[CrossRef](#)]
74. Zhou, T.; Geng, Y.; Ji, C.; Xu, X.; Wang, H.; Pan, J.; Bumberger, J.; Haase, D.; Lausch, A. Prediction of soil organic carbon and the C: N ratio on a national scale using machine learning and satellite data: A comparison between Sentinel-2, Sentinel-3 and Landsat-8 images. *Sci. Total Environ.* **2021**, *755*, 142661. [[CrossRef](#)] [[PubMed](#)]
75. Ziliani, M.G.; Altaf, M.U.; Aragon, B.; Houborg, R.; Franz, T.E.; Lu, Y.; Sheffield, J.; Hoteit, I.; McCabe, M.F. Early season prediction of within-field crop yield variability by assimilating CubeSat data into a crop model. *Agric. For. Meteorol.* **2021**, *313*, 108736. [[CrossRef](#)]
76. Li, F.; Miao, Y.; Chen, X.; Sun, Z.; Stueve, K.; Yuan, F. In-season prediction of corn grain yield through PlanetScope and Sentinel-2 images. *Agronomy* **2022**, *12*, 3176. [[CrossRef](#)]
77. Rouault, P.; Courault, D.; Pouget, G.; Flamain, F.; Diop, P.-K.; Desfonds, V.; Doussan, C.; Chanzy, A.; Debolini, M.; McCabe, M.; et al. Phenological and biophysical Mediterranean orchard assessment using ground-based methods and Sentinel 2 data. *Remote Sens.* **2024**, *16*, 3393. [[CrossRef](#)]
78. Rouault, P.; Courault, D.; Flamain, F.; Pouget, G.; Doussan, C.; Lopez-Lozano, R.; McCabe, M.; Debolini, M. High-resolution satellite imagery to assess orchard characteristics impacting water use. *Agric. Water Manag.* **2024**, *295*, 108763. [[CrossRef](#)]
79. Elfarkh, J.; Johansen, K.; El Hajj, M.M.; Almashharawi, S.K.; McCabe, M.F. Evapotranspiration, Gross Primary Productivity, and Water Use Efficiency over a High-Density Olive Orchard Using Ground and Satellite-Based Data. *Agric. Water Manag.* **2023**, *287*, 108423. [[CrossRef](#)]
80. Padilla-Díaz, C.M.; Rodriguez-Dominguez, C.M.; Hernandez-Santana, V.; Perez-Martin, A.; Fernandes, R.D.M.; Montero, A.; García, J.M.; Fernández, J.E. Water status, gas exchange and crop performance in a super high density olive orchard under deficit irrigation scheduled from leaf turgor measurements. *Agric. Water Manag.* **2018**, *202*, 241–252. [[CrossRef](#)]
81. Rodenhizer, H.; Yang, Y.; Fiske, G.; Potter, S.; Windholz, T.; Mullen, A.; Watts, J.D.; Rogers, B.M. A Comparison of Satellite Imagery Sources for Automated Detection of Retrogressive Thaw Slumps. *Remote Sens.* **2024**, *16*, 2361. [[CrossRef](#)]

**Disclaimer/Publisher’s Note:** The statements, opinions and data contained in all publications are solely those of the individual author(s) and contributor(s) and not of MDPI and/or the editor(s). MDPI and/or the editor(s) disclaim responsibility for any injury to people or property resulting from any ideas, methods, instructions or products referred to in the content.